# Supporting information

## Catalytic oxidation mechanism of ethyl acetate on O-ligand-single-atom-Ni/2 dimensional reduced graphene oxide: the essential role of O ligand

*Xinjie Wang[a], Juntian Li[b], Juan Li[b], Binghua Jing[b], Yun Sun[a], Teng Wang[a], Didi Li[a], Haibao Huang[c], Zhimin Ao[a,b,*]*

[a] Guangdong Key Laboratory of Environmental Catalysis and Health Risk Control, Institute of Environmental Health and Pollution Control, School of Environmental Science and Engineering, Guangdong University of Technology, Guangzhou 510006, China

[b] Advanced Interdisciplinary Institute of Environment and Ecology, Guangdong Provincial Key Laboratory of Wastewater Information Analysis and Early Warning, Beijing Normal University, Zhuhai 519087, PR China

[c] School of Environmental Science and Engineering, Sun Yat-sen University, Guangzhou 510275, China.

## Details of preparation of $SANi_X$-O-2DRGO

First, dispersing GO in aqueous solution obtained solution A of 10 mg/ml. Mixing nickel salt with water ultrasonic can obtain solution B of 10 mg/ml. Solution B with a certain gradient was mixed and stirred for 12 hours with 20 ml of solution A. Under the stirring condition, 5 ml of fresh sodium borohydride solution prepared on site was added. The stirring continued until the reaction was complete, and solution C was obtained. Solution C was extracted and separated by a 0.26μm water filter membrane to obtain the complex. The complex was repeatedly washed with deionized water and dried at 80℃ for 12 hours to obtain the high dispersion and high loading SANiX-O-2DRGO (X=0.5~5).

## Catalysis characterizations of $SANi_X$-O-2DRGO

The D8 ADVANCE X-ray Diffraction (XRD) is produced from Bruker, Germany. In the experiment, the scanning angles and rates are 5~90°and 2°/min, respectively. The iS50R of Fourier transform infrared spectroscopy (FTIR) is produced by Thermo Fisher, USA. And the experimental spectral band of FTIR is in the range of 400~4000 $cm^{-1}$. In-situ diffuse reflectance infrared fourier transform spectroscopy (XPS) is used to study the elemental species, chemical valence, and elemental content of the materials. The pore structure and surface area of the materials are characterized by BELSORP-max II, Japan. LabRAM HR Evolution Raman spectrometer (Raman) is from HORIBA Jobin Yvon, France, which is used to characterize the location of defects in the samples. Hydrogen-Programmed Temperature Reductions ($H_2$-TPR) are carried out on samples by using the TP-5078 Atochem chemisorption/desorption instrument manufactured by Pioid, China. The thermal stability of various samples is investigated by using the Thermogravimetric analyzer (TGA), which is manufactured by Mettler-Toledo, Switzerland. The Field emission transmission electron microscopy (FE-TEM) and the high resolution transmission electron microscopy (HR-TEM) are Talos F200S from FEI, Czech Republic.

## Results and Discussion

The XRD pattern is shown in Figure S5, all peaks of $SANi_X$-O-2DRGO (X=0.5~5) remain highly consistent, containing mainly two typical diffraction peaks at 2θ=24.7° and 40.4°. It is noteworthy that an additional small carbon (100) peak is presented around 2θ=40.4°, related to the degree of condensation of the carbon structure[1, 2]. No Ni species related diffraction peaks are observed for any of the $SANi_X$-O-2DRGO (X=0.5~5) due to the low loading of Ni, which is consistent with no metal clusters being observed in the TEM images. The TGA profile of the $SANi_X$-O-2DRGO (X=0.5~5) is presented in Figure S6, no significant weight loss steps were observed during the room temperature to 600 °C. The weight loss below 300 °C is less than 10%, implying that the catalyst is thermally stable and suitable for thermal catalysis experiments.

The Brunauer–Emmett–Teller (BET) is used to characterize the surface area and pore volume of $SANi_X$-O-2DRGO (X=0.5~5). As shown in Figure S7, all samples have a similar V-shaped isotherm with an H2a-type hysteresis loop. H2a-type hysteresis loop production is due to cavitation controlled evaporation of the pore size within a narrow range during desorption, and perhaps the presence of pore blockage or percolation[3]. The pore diameter of $SANi_X$-O-2DRGO (X=0.5~5) is in the range of 6.42~17.39 nm. The specific surface area of $SANi_X$-O-2DRGO (X=1~5) is above 90 $m^2$ $g^{-1}$ except $SANi_{0.5}$-O-2DRGO (Table S3). This is related to the low metal content of $SANi_{0.5}$-O-2DRGO, which leads to a small gap between RGO layers [4]. ICP-MS was used to characterize the content of Ni elements in the materials. The results are shown in Table S4, Ni content of the samples tended to increase with the addition of the $NiCl_2$•$6H_2O$. The actual contents of $SANi_X$-O-2DRGO (X=0.5~5) are 0.73%, 1.86%, 3.43%, 5.44%, 8.13% and 10.16%, respectively. The metal content of single atom catalysts is generally extremely low [5-8]. Interestingly, the $SANi_5$-O-2DRGO remains atomically distributed with high Ni loading.

The $H_2$-TPR characterized the redox ability of the $SANi_X$-O-2DRGO (X=0.5~5). As shown in Figure S11, with the increase of metal loading the reduction temperature of $SANi_X$-O-2DRGO (X=0.5~5) is almost constant, while the intensity of the reduction peaks is rising. Interestingly, the $SANi_X$-O-2DRGO (X=3~5) samples show a more intense peak at 397°C, which is produced by the reduction of Ni(II), corresponding to the reduction peak of the higher valence nickel ions [9]. $SANi_X$-O-2DRGO (X=1~2) shows the same reduction peak at the same position, but with a less intense peak. At the same time, $SANi_{0.5}$-O-2DRGO also shows a small reduction peak at the same position, while RGO shows no peak at this position. Although there are no clear changes in the overall peak position, the intensity of overall peaks is consistent with the change in the catalytic performance of ethyl acetate, with $SANi_5$-O-2DRGO > $SANi_4$-O-2DRGO > $SANi_3$-O-2DRGO > $SANi_2$-O-2DRGO ≈ $SANi_1$-O-2DRGO > $SANi_{0.5}$-O-2DRGO > RGO. Therefore, it is presumed that the single Ni atoms loaded on the RGO are the active site for the catalytic reaction, and it is demonstrated that the catalytic activity increases with the increase in metal loading. Used and fresh $SANi_5$-O-2DRGO presented typical carbon features with distinct D bonds and G bonds in the Raman spectra (Figure S12). The ratio of D band intensity to G band intensity (ID/IG) for used $SANi_5$-O-2DRGO is 1.27, approximately equal to 1.42 for fresh $SANi_5$-O-2DRGO, indicating defects hardly participate in the catalytic oxidation reaction [10].

Ethyl acetate-temperature-programmed desorption (TPD) was investigated. In the experiment, helium was introduced at 150°C for 1 hour before pretreatment, and ethyl acetate was introduced for adsorption for 2 hours. The temperature was programmed under helium. The control group was treated with helium gas. From the Figure S15, it can be concluded that the maximum desorption rate of ethyl acetate is reached at 85 ° C.

The kinetic studies are calculated. The calculation steps are shown as follows:

The conversion of ethyl acetate was calculated by equation (1):

$$X_{VOCs}\% = \frac{C_0 - C_t}{C_0} \times 100\%$$

where $C_0$ and $C_t$ represent ethyl acetate concentration in the inlet and outlet gas, respectively.

The reaction rate was calculated as equation (2):

$$r_{VOCs}\% = \frac{X_{VOCs} - V_{VOCs}}{M_{cat} w\%_{Ni}}$$

where $V_{VOCs}$ represents the feed gas flow rate (mol/s), $M_{cat}$ represents the catalyst weight (g), $w\%_{Ni}$ is the content of Ni in catalyst (%).

The activation energy $E_a$ can be determined from the Arrhenius equation (3):

$$lnr = \frac{-E_a}{RT} + lnA$$

where R is the universal constant with a value of 8.314 x $10^{-3}$ kJ/mol·K, A is a constant, and T is the temperature (in Kelvin).

In order to explore the intrinsic activity of the catalyst and the kinetic changes of the catalytic process, the ordinate of $lnr$ and the abscissa of $1000/T$ were respectively considered, and the relevant reaction activation energy ($E_a$) was calculated by Arrhenius equation. The data points were selected for kinetic analysis under the condition that the conversion rate of ethyl acetate was maintained within 5%. As depicted in Figure S16, As the activation energy over the $SANi_5$-O-2DRGO is 21.8 kJ/mol, which substantially lower than other reported catalysts.

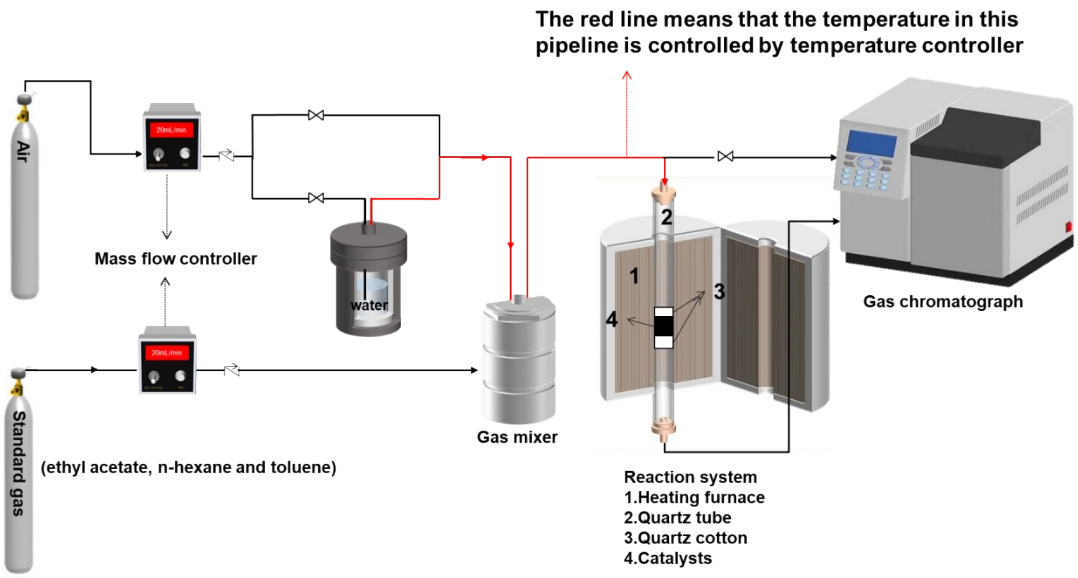


Figure S1. The setup schematic of the experiment

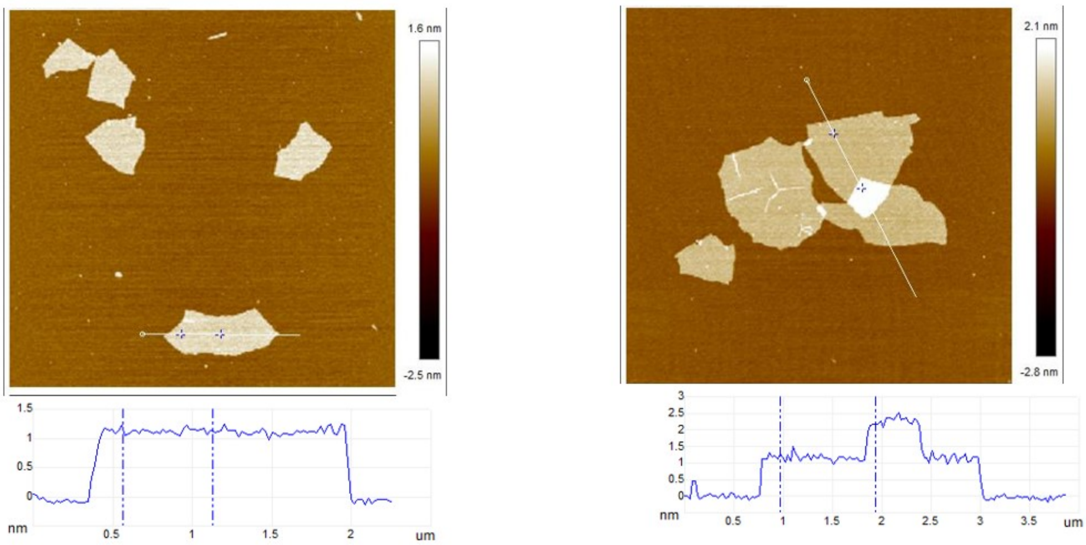


Figure S2. The Atomic force microscopy (AFM) images of GO

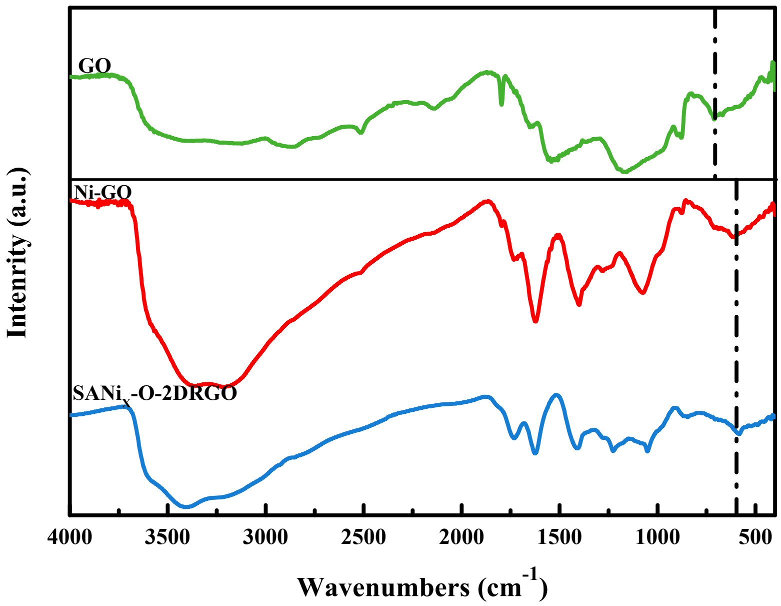


Figure S3. The infrared spectra of SANi$_5$-O-2DRGO, graphene oxide, and unreduced Ni-GO mixtures

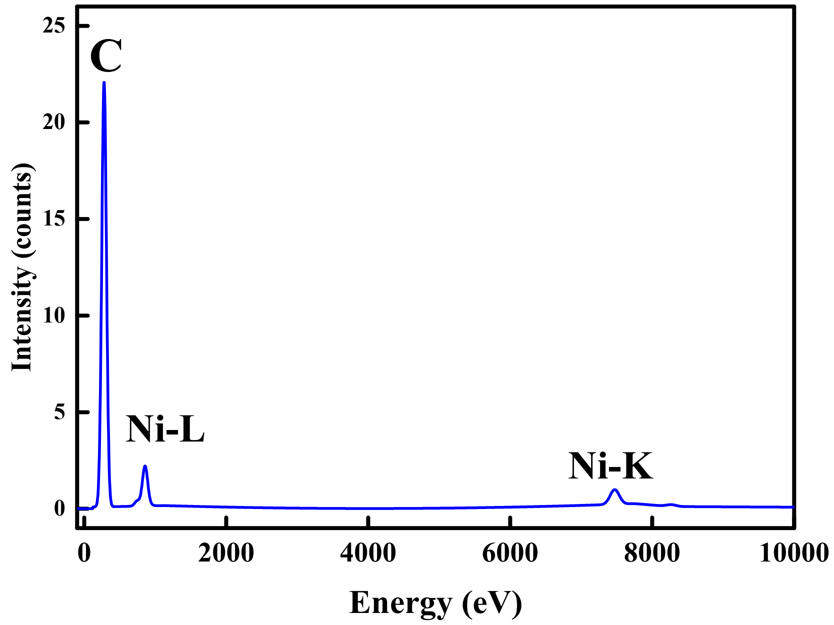


Figure S4. The surface sweep energy dispersive spectroscopy of SANi$_5$-O-2DRGO

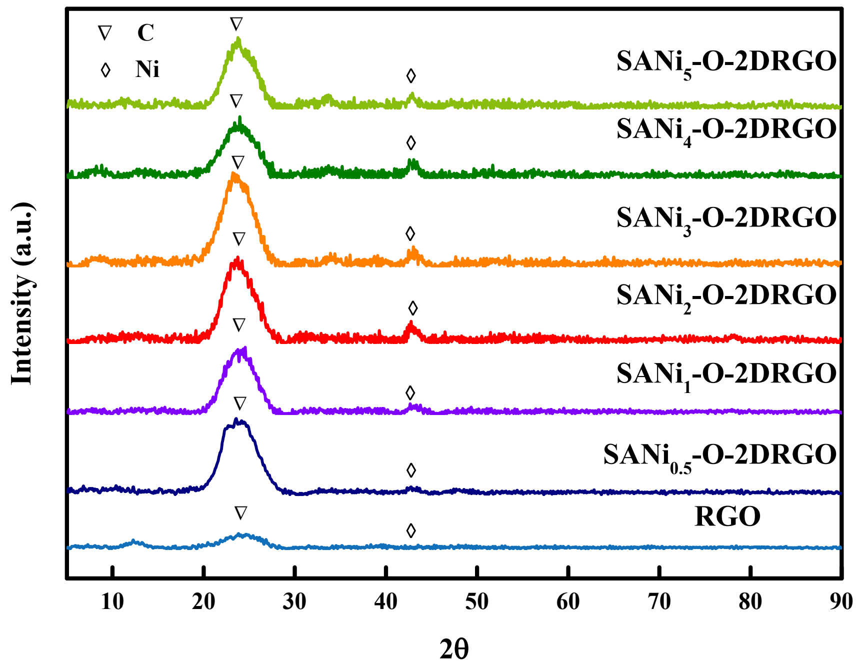


Figure S5. XRD patterns of SANi$_X$-O-2DRGO

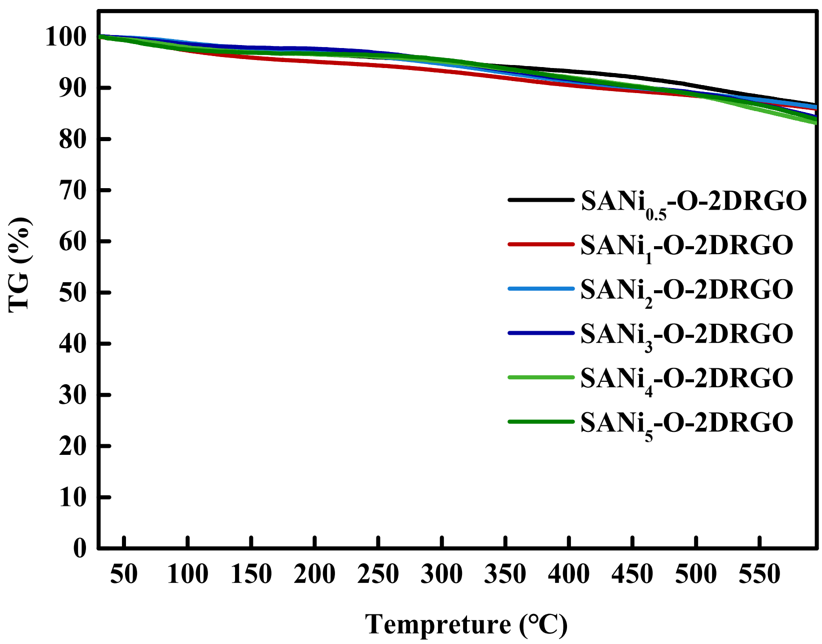


Figure S6. TGA curves of $SANi_X$-O-2DRGO

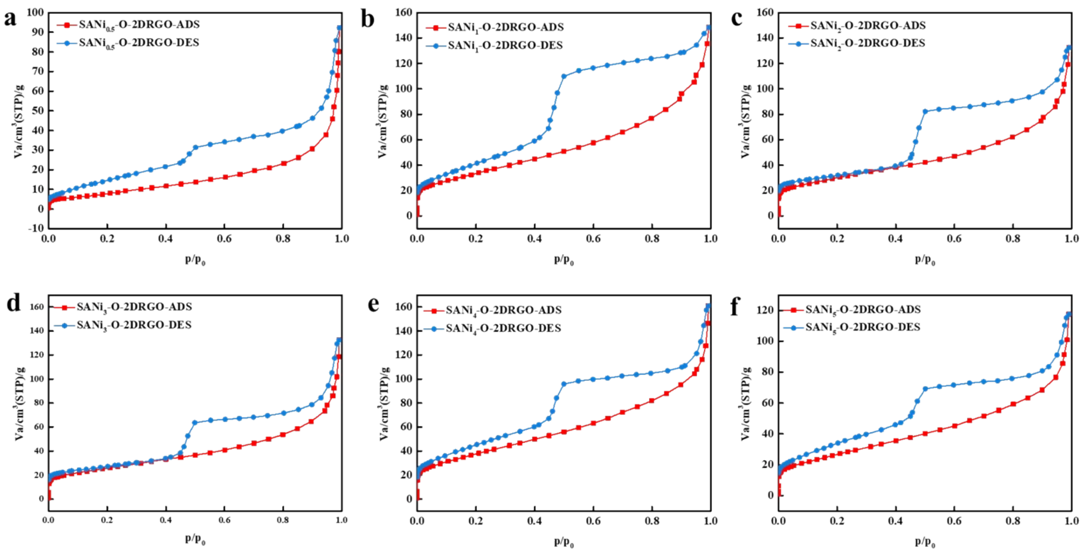


Figure S7. Nitrogen-sorption isotherms of $SANi_X$-O-2DRGO

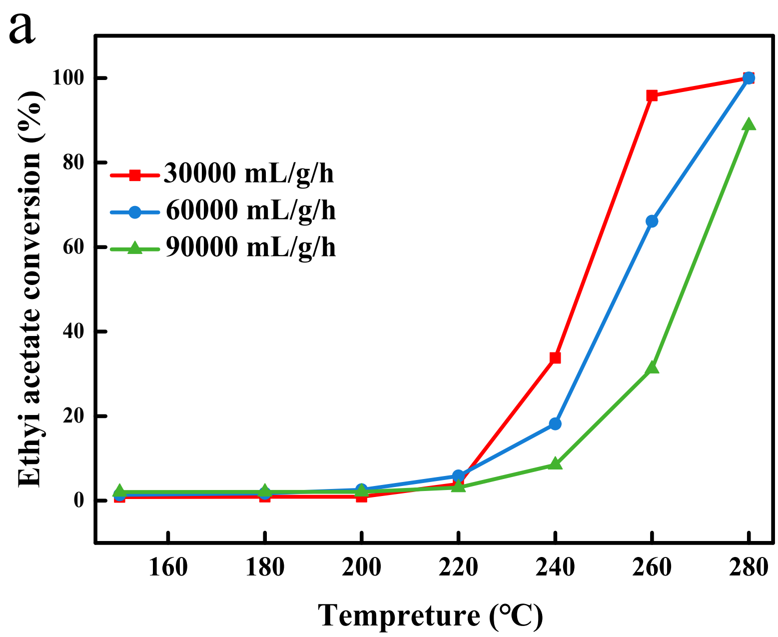


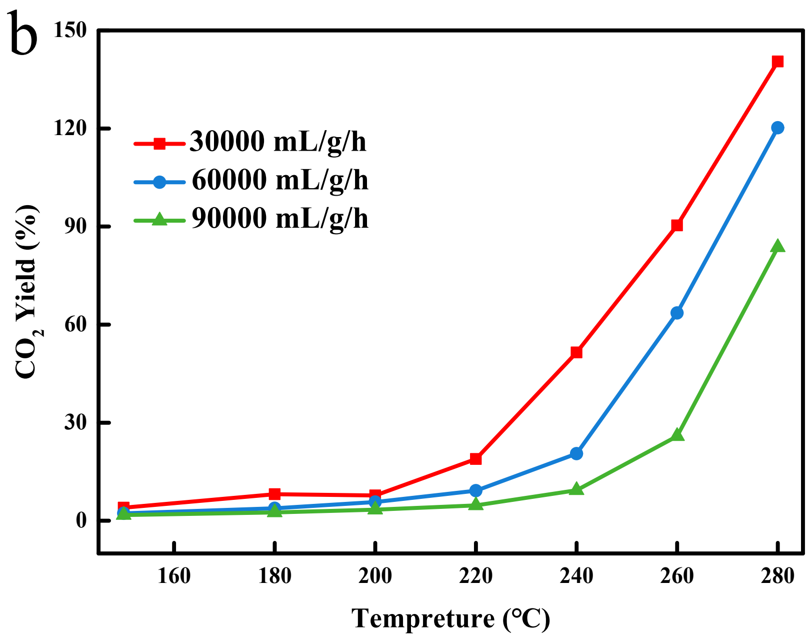


Figure S8. Conversion of ethyl acetate (a) and $CO_2$ yield (b) at different WHSV

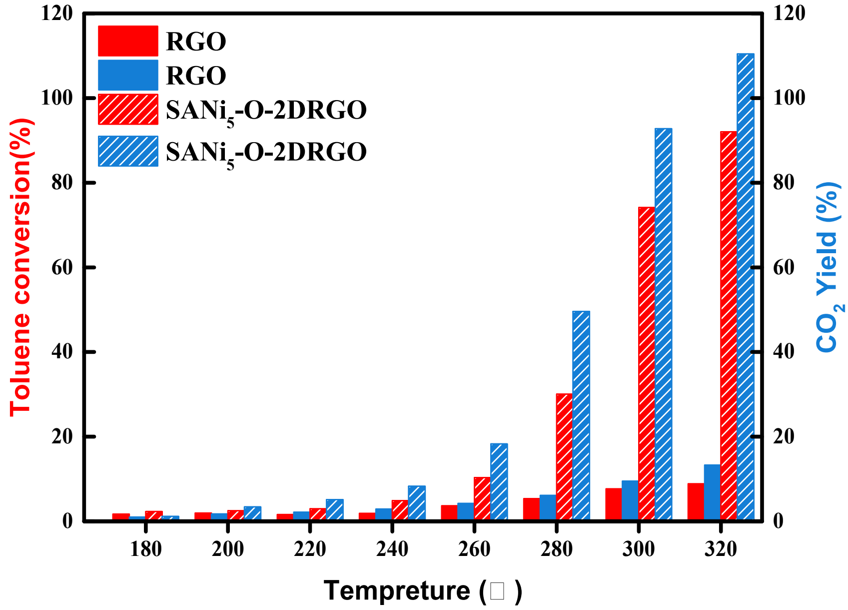


Figure S9. Conversion of toluene and $CO_2$ yield over SANi$_5$-O-2DRGO

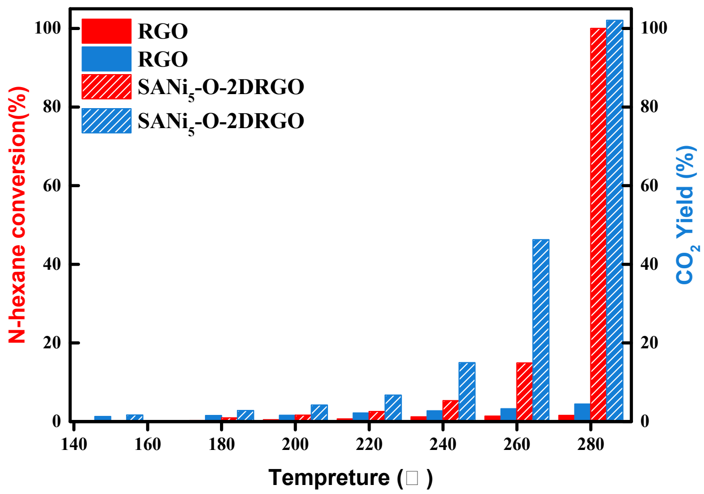


Figure S10. Conversion of n-hexane and $CO_2$ yield over SANi$_5$-O-2DRGO

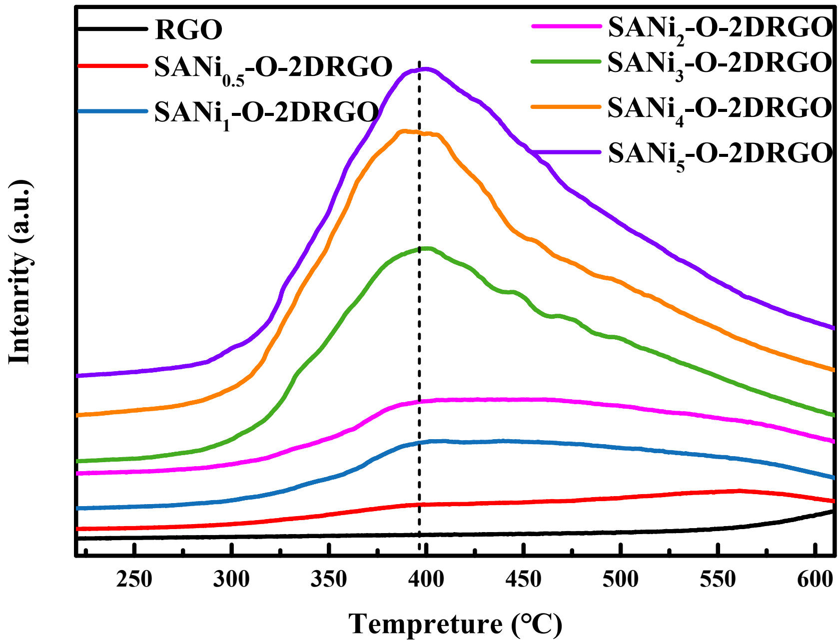


Figure S11. The $H_2$-TPR profiles of $SANi_X$-O-2DRGO

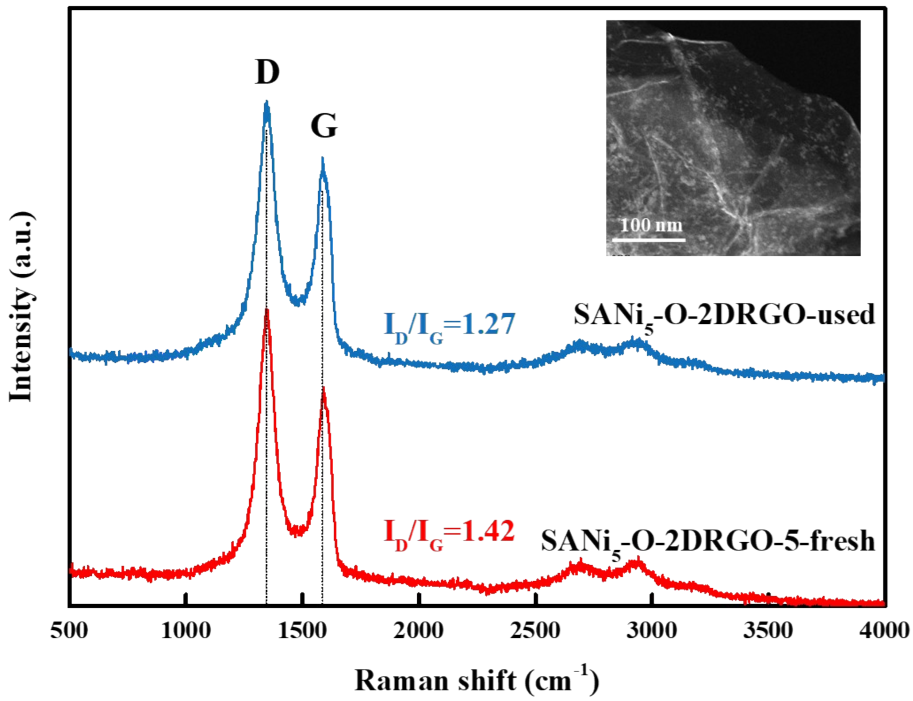


Figure S12. The Raman spectra of $SANi_5$-O-2DRGO-used/fresh

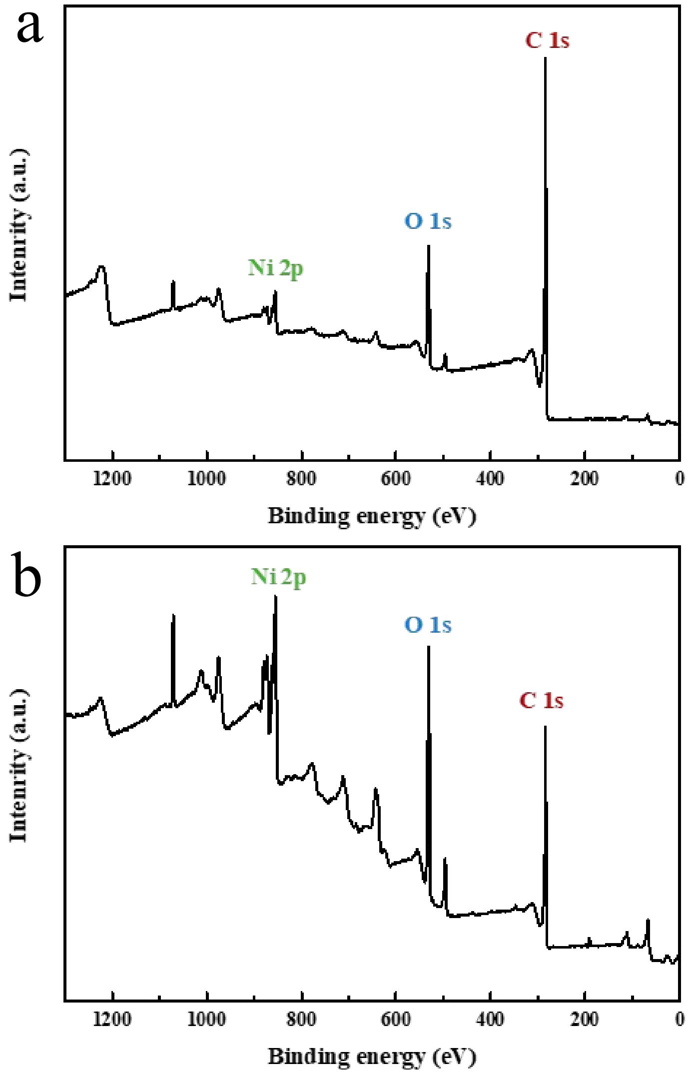


Figure S13. Split peak fit plots of the C1s peak, O1s peak, and Ni 2p peak of fresh and used $SANi_5$-O-2DRGO

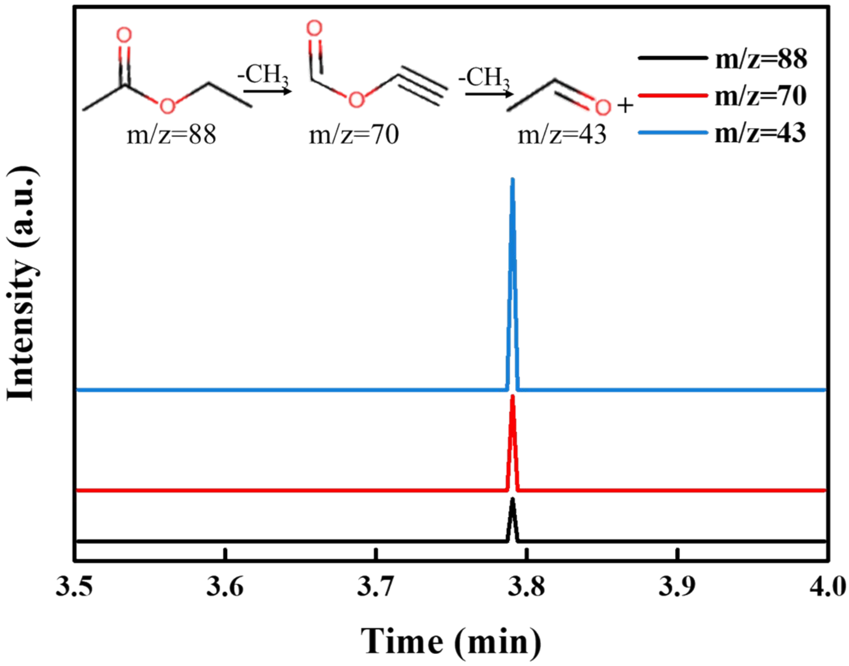


Figure S14. The mass spectroscopy of ethyl acetate over $SANi_5$-O-2DRGO

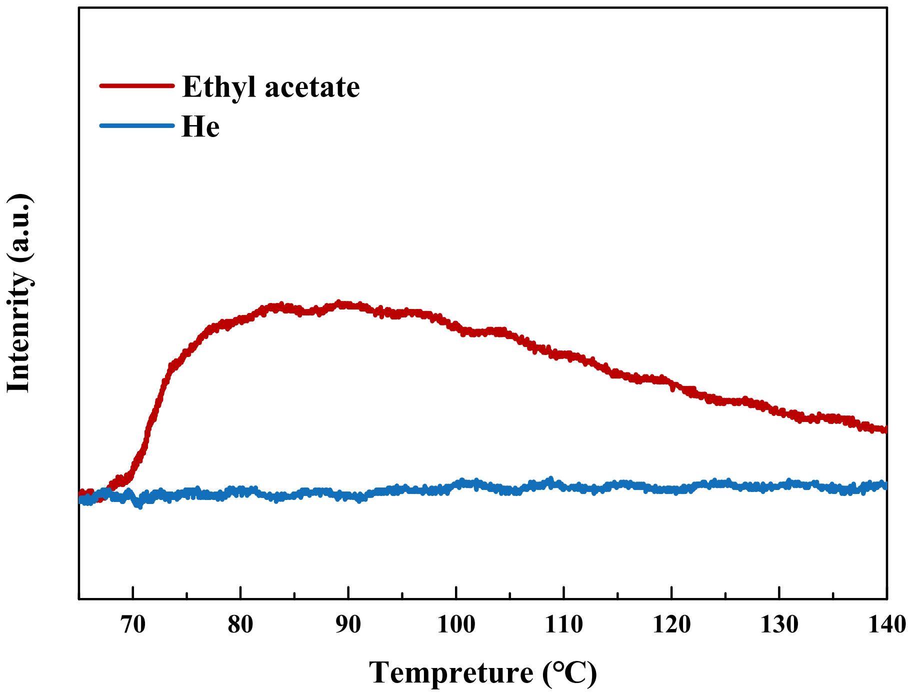


Figure S15. Ethyl acetate-TPD and He-TPD of $SANi_5$-O-2DRGO

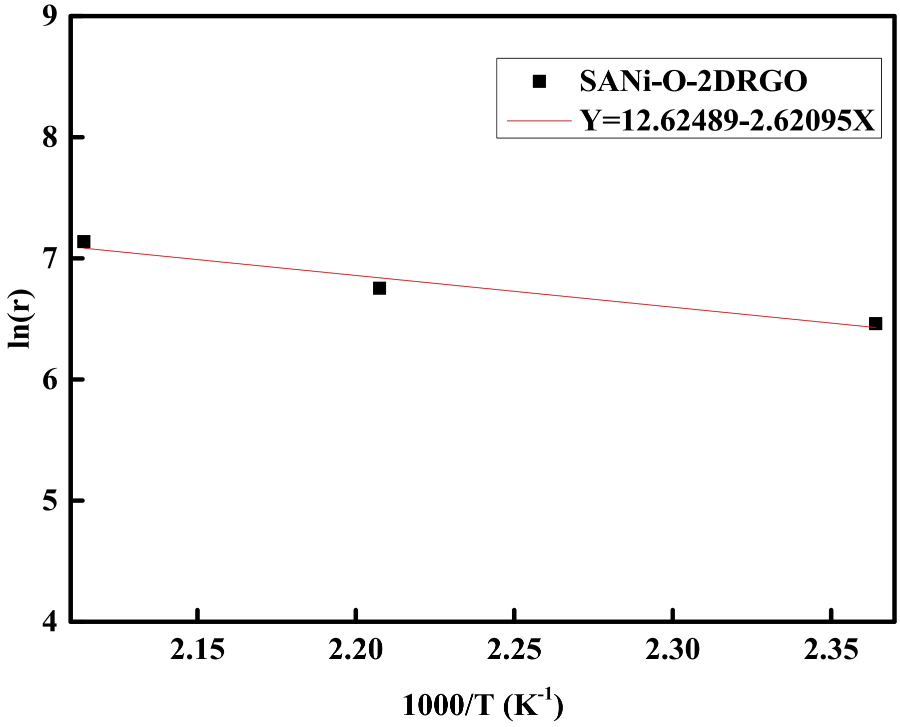


Figure S16. Arrhenius plots over $SANi_5$-O-2DRGO in the ethyl acetate oxidation reaction

Table S1. The EXAFS fitting results of $SANi_5$-O-2DRGO

| Catalysts | Path | N | R (Å) | $\sigma^2$ (Å$^2$) | $\Delta E_0$ (eV) | R-factor |
|---|---|---|---|---|---|---|
| $SANi_5$-O-2DRGO | Ni-O | 4.0 | 1.6 | 0.011 | -8.29 | 0.003 |

Table S2. The Fukui values (f -) of ethyl acetate

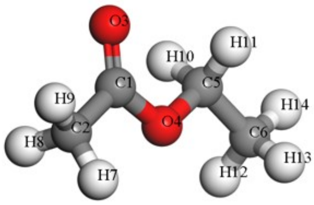


| Atom | C1 | C2 | O3 | O4 | C5 | C6 | H7 |
|---|---|---|---|---|---|---|---|
| *f*(+) | 0.25 | -0.05 | 0.23 | 0.09 | -0.06 | -0.02 | 0.10 |
| *f*(-) | 0.10 | -0.01 | 0.40 | 0.11 | -0.08 | -0.02 | 0.10 |
| **Atom** | **H8** | **H9** | **H10** | **H11** | **H12** | **H13** | **H14** |
| *f*(+) | 0.13 | 0.09 | 0.06 | 0.06 | 0.04 | 0.04 | 0.06 |
| *f*(-) | 0.09 | 0.07 | 0.05 | 0.05 | 0.04 | 0.04 | 0.06 |

Table S3. The BET results of $SANi_X$-O-2DRGO

| Catalysts | $V_p$ ($cm^3\ g^{-1}$) | $D_{average}$ (nm) | $S_{BET}$ ($m^2\ g^{-1}$) |
|---|---|---|---|
| $SANi_{0.5}$-O-2DRGO | 0.1423 | 17.39 | 32.587 |
| $SANi_1$-O-2DRGO | 0.2223 | 7.01 | 125.75 |
| $SANi_2$-O-2DRGO | 0.1870 | 7.05 | 107.91 |
| $SANi_3$-O-2DRGO | 0.1901 | 7.92 | 92.825 |
| $SANi_4$-O-2DRGO | 0.2432 | 6.72 | 139.36 |
| $SANi_5$-O-2DRGO | 0.1727 | 6.42 | 100.03 |

Table S4 The ICP-MS results of $SANi_X$-O-2DRGO

| Catalysts | $SANi_{0.5}$-O-2DRGO | $SANi_1$-O-2DRGO | $SANi_2$-O-2DRGO | $SANi_3$-O-2DRGO | $SANi_4$-O-2DRGO | $SANi_5$-O-2DRGO |
|---|---|---|---|---|---|---|
| ICP-MS | 0.73% | 1.86% | 3.43% | 5.44% | 8.13% | 10.16% |

Table S5. Information of all detected intermediates during the reaction

| Label | Molecular formula | Compound mane | Molecular structure | Ion debris (m/z) |
|---|---|---|---|---|
| 1 | $C_4H_8O_2$ | Ethyl acetate | 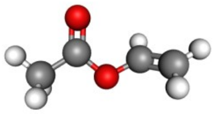 | 15, 26, 27, 43, 86, 87 |
| 2 | $C_2H_4O_2$ | Acetic acid | 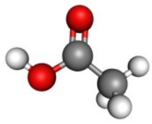 | 14, 15, 16, 43, 45, 60 |
| 3 | $C_2H_6O$ | Ethanol | 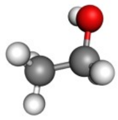 | 12, 13, 31, 45, 46 |
| 4 | $C_2H_4O$ | Acetaldehyde | 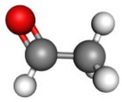 | 14, 29, 42, 43, 44 |
| 5 | $C_2H_2O$ | Ketene | 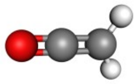 | 14, 16, 24, 25, 41, 42 |
| 6 | $C_2H_2$ | Ethylene | 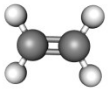 | 14, 15, 16, 28, 29, 30 |
| 7 | $CH_2O_2$ | Formic acid | 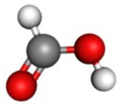 | 17, 29, 45, 46 |
| 8 | $CO_2$ | Carbon oxide | 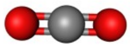 | 12, 16, 28, 44 |
| 9 | $H_2O$ | Water | 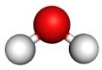 | 18 |

## REFERENCES

[1] T. Qiu, J.G. Yang, X.J. Bai, Y.L. Wang, The preparation of synthetic graphite materials with hierarchical pores from lignite by one-step impregnation and their characterization as dye absorbents, RSC Adv, 9 (2019) 12737-12746.
[2] Z. Abbasi, M. Haghighi, E. Fatehifar, S. Saedy, Synthesis and physicochemical characterizations of nanostructured Pt/Al2O3–CeO2 catalysts for total oxidation of VOCs, Journal of Hazardous Materials, 186 (2011) 1445-1454.
[3] Z. Alothman, A Review: Fundamental Aspects of Silicate Mesoporous Materials,

Materials, 5 (2012) 2874-2902.
[4] I. Esteve-Adell, M. Porcel-Valenzuela, L. Zubizarreta, M. Gil-Agusti, M. Garcia-Pellicer, A. Quijano-Lopez, Influence of the Specific Surface Area of Graphene Nanoplatelets on the Capacity of Lithium-Ion Batteries, Front Chem, 10 (2022) 807980.
[5] Z. Abbasi, M. Haghighi, E. Fatehifar, S. Saedy, Synthesis and physicochemical characterizations of nanostructured Pt/Al2O3-CeO2 catalysts for total oxidation of VOCs, J Hazard Mater, 186 (2011) 1445-1454.
[6] D. Yang, S. Fu, S. Huang, W. Deng, Y. Wang, L. Guo, T. Ishihara, The preparation of hierarchical Pt/ZSM-5 catalysts and their performance for toluene catalytic combustion, Microporous and Mesoporous Materials, 296 (2020).
[7] J. Zhang, C. Rao, H. Peng, C. Peng, L. Zhang, X. Xu, W. Liu, Z. Wang, N. Zhang, X. Wang, Enhanced toluene combustion performance over Pt loaded hierarchical porous MOR zeolite, Chemical Engineering Journal, 334 (2018) 10-18.
[8] R. Peng, S. Li, X. Sun, Q. Ren, L. Chen, M. Fu, J. Wu, D. Ye, Size effect of Pt nanoparticles on the catalytic oxidation of toluene over Pt/CeO2 catalysts, Applied Catalysis B: Environmental, 220 (2018) 462-470.
[9] Z. Hou, Characterization of Ca-promoted Ni/α-$Al_2O_3$ catalyst for $CH_4$ reforming with $CO_2$, *Appl. Catal.A.*, 253 (2003) 381-387.
[10] J. Wu, J. Wang, C. Liu, C. Nie, T. Wang, X. Xie, J. Cao, J. Zhou, H. Huang, D. Li, S. Wang, Z. Ao, Removal of gaseous volatile organic compounds by a multiwalled carbon nanotubes/peroxymonosulfate wet scrubber, *Environ. Sci. Technol.*, 56 (2022) 13996-14007.
[11] B. Niu, Y. Wang, T. Zhao, X. Duan, W. Xu, Z.Y. Zhao, Z.W. Yang, G.G. Li, J.F. Li, J. Cheng, Z.P. Hao, Modulating the Electronic States of Pt Nanoparticles on Reducible Metal-Organic Frameworks for Boosting the Oxidation of Volatile Organic Compounds, Environmental Science & Technology, (2024) 4428-4437.